Applied Catalysis B: Environmental 160–161 (2014) 98–105

Contents lists available at ScienceDirect

Applied Catalysis B: Environmental

journal homepage: www.elsevier.com/locate/apcatb

Au deposited BiOCl with different facets: On determination of the facet-induced transfer preference of charge carriers and the different plasmonic activity

Huaxiang Lin*, Luyao Ding, Zengxia Pei, Yangen Zhou, Jinlin Long, Weihua Deng, Xuxu Wang*

Research Institute of Photocatalysis, State Key Laboratory of Photocatalysis on Energy and Environment, Fuzhou University, Fuzhou 350002, PR China

ARTICLE INFO

Article history:
Received 11 February 2014
Received in revised form 28 April 2014
Accepted 11 May 2014
Available online 16 May 2014

Keywords:
BiOCl
Au nanoparticle
Facet
Surface plasmon resonance
Photocatalytic

ABSTRACT

By deposition of Au nanoparticles (Au NPs) onto BiOCl (BOC) nanosheet with different facets, in the reaction of decomposing Orange II, we systematically investigated the preferred transfer orientation (PTO) of photo-generated electron–hole pairs in BOC under UV light irradiation. Also, the active oxidative intermediates during the degradation process were also studied. Moreover, the Au NPs successfully brought about visible light response to the wide gap BOC, while the exposed different facets were found to be influential on the surface plasmon resonance (SPR) effect. The present work may contribute to a deeper sight of the relationship between specific facets and photocatalytic performance, together with a further understanding of SPR-induced photocatalytic activity.

1. Introduction

Heterogeneous semiconductor photocatalysis is a promising approach for easing worldwide environmental and energy-related problems by effective utilization of solar energy [1–3]. Photo-generated electron–hole (e^-–h^+) pairs are fundamentally active species in photocatalytic reactions and a good separation of the charge carriers can remarkably boost the overall photocatalytic efficiency. It has been demonstrated that anistropic shaped particles could retard the fast recombination of e^-–h^+ pairs owing to their intrinsic geometric and electronic properties [4–6]. Additionally, there exists the PTO of photo-generated electron and hole in different crystal facets due to the subtle distinction of coupled facets, which benefits the separation of charge carriers [7,8]. Therefore, a comprehensive and in-depth understanding of the facet-oriented separation of charge carriers will evidently contribute to the fabrication of highly efficient photocatalyst.

BiOCl, as a wide-band semiconductor photocatalyst, is widely investigated because of its broad applications in many areas [9–12]. Recently, the surface structure of BiOCl photocatalyst has been explored at atomic level [13–15]. A breakthrough has been made by Zhang et al. [14], who reported the facet-controllable synthesis of BiOCl single-crystalline nanosheets (BOC SCNSs) with exposed (0 0 1) and (0 1 0) facets. However, the PTO of photo-generated electron and hole in BiOCl is still of uncertainty. Besides, no utilization of visible light and low quantum efficiency of this photocatalyst remain two major barriers which hold back its application on large scale. On the other hand, it is revealed that the photocatalytic activity can be dramatically enhanced by loading a small amount of Au NPs on semiconductor photocatalyst, because electrons on the conduction band of the semiconductor would transfer to Au NPs due to the Schottky barrier effect [16–18]. This fact inspires us that Au NPs may act as a probe to determine the PTO of photo-induced charge carriers, as Au NPs will facilitate the transfer of electrons on electron-preferred (reductive) facet or cause recombination of e^- and h^+ on hole-preferred (oxidative) facet. Moreover, Au NPs exhibit unique optical properties that arise from resonant oscillation of free electrons upon interaction with electromagnetic radiation, which is known as the localized SPR effect [16,18–20]. This phenomenon will cause an obvious absorption at approximately 550 nm and could promisingly endow wide-gap materials with visible-light response. Nonetheless, the detailed mechanism of SPR effect in photocatalytic degradation process is still not fully understood, as some recent works [21,22] report that the substrate could intensely affect the deposited noble metal. Thus, further study is highly desired to look into the influence of support on the SPR effect.

* Corresponding author. Tel.: +86 591 8377 9251; fax: +86 591 8377 9251.
E-mail addresses: lhx@fzu.edu.cn (H. Lin), xwang@fzu.edu.cn (X. Wang).

http://dx.doi.org/10.1016/j.apcatb.2014.05.018
0926-3373/

In the present study, BOC SCNS samples with high percentage exposure of (0 0 1) and (0 1 0) facets were synthesized through a facile reported hydrothermal method [14]. By detecting the generation of $O_2^{\bullet-}$ and $^{\bullet}OH$ species, and further depositing Au NPs onto the BOC SCNSs, we systematically investigated the charge separation mechanism between (0 0 1) and (0 1 0) facets. It is demonstrated that electrons and holes will transfer spontaneously toward (0 0 1) and (0 1 0) facet respectively, and this separation can be facilitated/deteriorated by deposition of Au NPs on {0 0 1}/{0 1 0} facets. Simultaneously, SPR effect of the deposited Au NPs also renders BOC SCNSs with remarkable visible light activity, and the different facets were found to affect the SPR effect. It is hoped that our work may help better understanding of the facet-induced charge separation in BOC materials, and also provide a new insight into the effect of different substrates over the SPR action.

2. Experimental

2.1. Materials

Bismuth nitrate pentahydrate ($Bi(NO_3)_3{\cdot}5H_2O$), potassium chloride (KCl), chloroauric acid tetrahydrate ($AuCl_3{\cdot}HCl{\cdot}4H_2O$), sodium hydroxide (NaOH), sodium borohydride ($NaBH_4$), Orange II ($C_{16}H_{11}N_2NaO_4S$), nitroblue tetrazolium (NBT), terephthalic acid (TA), N,N-diethyl-p-phenylenediamine (DPD), horseradish peroxidase (POD) and ethanol were all obtained from Sinopharm Chemical Reagent Co. Ltd., and all of these reagents were analytical pure and were used without further purification. Deionized water was used throughout the work.

2.2. Synthesis of BiOCl with exposed (0 0 1) and (0 1 0) facets

BOC SCNSs with dominant exposed (0 0 1) and (0 1 0) facets were synthesized by modifying a reported method [14]. 4 mM of $Bi(NO_3)_3{\cdot}5H_2O$ and 4 mM of KCl were added in 70 mL deionized water at room temperature under continuous stirring. NaOH was used to adjust the pH value of solution (pH = 6.0). After stirring for 0.5 h, the mixture solution was decanted into a 100 mL Teflon-lined stainless autoclave. The autoclave was then heated at 120 °C for 24 h under autogenous pressure, and then cooled to room temperature naturally. The resulting sediments were gathered and rinsed with deionized water thoroughly and then dried at 60 °C in oven. The obtained sample was marked as BOC-010. By contrast, the product without adding NaOH was marked as BOC-001.

2.3. Synthesis of Au-loaded BiOCl

Au-loaded BOC-010 photocatalyst was prepared by impregnation followed by a reduction process. Typically, 2 g BOC-010 sample was impregnated in $HAuCl_4$ solution (Au 0.01 g/mL) with an appropriate volume and then dried at 120 °C for 6 h in vacuum. The resulting powders were reduced by 0.02 M $NaBH_4$ solution, then centrifugated, washed thoroughly with distilled water, and finally dried at 60 °C overnight. The gold content of the sample was estimated to be 0.7 wt% by the precursor feeding. The Au/BOC-001 was synthesized by the same procedure.

2.4. Characterization

Crystal structure identification was performed using Bruker D8 X-ray diffractometer (XRD) with Cu K_α radiation operating at 40 kV and 40 mA. The morphologies of BOC SCNSs were observed by an FEI Nova NanoSEM 230 field-emission scanning electron microscope (SEM). Microstructures and selected area electron diffraction (SAED) patterns were investigated using TecnaiG2 F20 S-TWIN (FEI company) Transmission electron microscopy (TEM) with a field emission gun at 200 kV. X-ray photoelectron spectroscopy (XPS) analysis was conducted on an ESCALAB 250 photoelectron spectroscopy (Thermo Fisher Scientific) at 1.2×10^{-9} mbar using Al Kα X-ray beam (1486.6 eV). Diffuse reflection spectra (DRS) of the samples were recorded on a Varian Cary-500 spectrophotometer, using $BaSO_4$ as the reference. UV–vis spectra were measured on a UV–vis–NIR spectrometer (Cary-500). The photoluminescence (PL) spectra were obtained using an Edinburgh Analytical Instrument FL/FSTCSPC920 Spectrophotometer.

2.5. Photocatalytic activity test

The UV light photocatalytic activity of all the samples was estimated by degradation of Orange II under UV light irradiation. For all reactions, 10 mg photocatalyst was added into 80 mL of Orange II solution (20 ppm) in a quartz tube. Three UV lamps (4 W, Philips TUV 4 W/G4 T5) surrounded the tube reactor and provide illumination with a predominant wavelength at 254 nm (10 μW/cm^2). As for determining the visible light activity, 50 mg powers were put into pyrex glass reactor and 80 mL Orange II solution (5 ppm) was added. A 300 W Xe lamp was used with cut-off filter to provide visible light (>420 nm) only. Prior to irradiation, stirring in dark for 30 min was allowed for establishment of adsorption/desorption equilibrium. At given irradiation time intervals, 3 mL of the solution was taken out and centrifuged, then analyzed on the UV–vis spectrometer. The final efficiency was calculated by the following equation:

$$E_t \ (\%) = \left(\frac{1 - C_t}{C_0}\right) \times 100\%,$$

where C_0 and C_t stands for the concentration of reactants at initial and at a certain irradiation time t, respectively.

2.6. Reactive oxidative species (ROS) test

Superoxide radical ($O_2^{\bullet-}$) and hydroxyl radical ($^{\bullet}OH$) were measured by reported methods [22,23]. 20 mg powers were added into 80 mL of 2×10^{-5} M NBT (or TA (5 ppm) and NaOH (2×10^{-3} M) solution) in a quartz tube. Prior to irradiation, stirring in dark for 30 min was allowed for establishment of adsorption/desorption equilibrium. At given irradiation time intervals, 3 mL of the NBT solution was taken out and centrifuged, then analyzed by recording the maximum absorption band (259 nm for NBT) on the UV–vis spectrometer. The upper clear liquid of TA solution was analyzed by recording the maximum PL peak (426 nm for TAOH) with an excitation wavelength of 312 nm. Hydrogen peroxide was measured by the DPD/POD method [24]. 20 mg powers were added into 80 mL of water in a quartz tube. The upper solution was collected after 2 h period of UV irradiation. DPD and POD were subsequently added into the solution sample and then tested by UV–vis spectrometer.

2.7. Photoelectrochemical measurement

Photoelectrochemical characterization was conducted on a ZENNIUM electrochemical workstation (Zahner, Germany) with a standard three-electrode system. The prepared samples served as the working electrode with an active area of *ca.* 0.25 cm^2. The counter and reference electrodes were Pt plate and Ag/AgCl electrode and 0.2 M Na_2SO_4 (pH = 6.8) was used as electrolyte. A 300 W xenon lamp was used to provide UV light.

3. Results and discussion

3.1. Characterization of the Au deposited BOC samples

XRD patterns of the as-prepared pure BOC SCNSs and Au/BOC samples are shown in Fig. S1. All observed peaks can be well

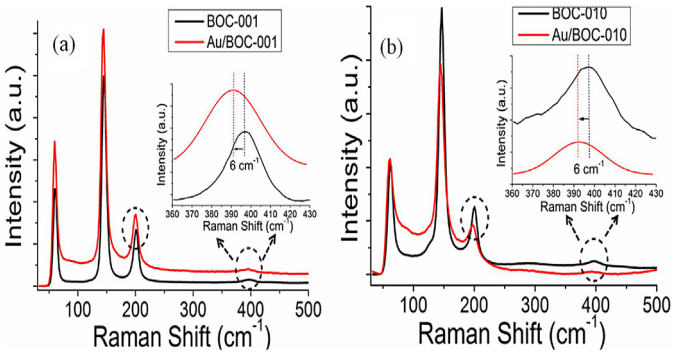

Fig. 1. Raman spectra of BOC samples with or without Au loading.

indexed to tetragonal phase BiOCl (JCPDS No. 01-082-0485), indicating good crystallization of the sample and that Au deposition did not make any change to the crystal structure of BOC. No Au peaks were detected, probably due to the low loading amount and small particle size of Au NPs, which also implies that Au NPs distributed uniformly onto the surface of BOC SCNSs [25,26]. To get an insight into the surface structure of the samples, Raman spectra were further recorded as exhibited in Fig. 1. Two intense bands centered at some 60 cm^{-1} and 145 cm^{-1} are assigned to the A_{1g} external and internal Bi–Cl stretching mode, respectively [27,28]. The band located at 199 cm^{-1} can be attributed to the E_g internal Bi–Cl stretching mode, while E_g external Bi–Cl one is probably masked by the strongest band at 145 cm^{-1} [28]. Another broad weak band, which is caused by the motion of the oxygen atoms at about 398 cm^{-1}, is related to E_g and B_{1g} modes. It is worth noting that the bands at 199 and 398 cm^{-1} have a blue-shift for 6 cm^{-1}. This phenomenon is known as the result of light-induced compressive stress in the Au/BOC SCNSs system [29]. In detail, Au NPs can absorb photons when Au/BOC sample is irradiated by 532 nm light provided by Raman spectrometer. Then the photo-generated electrons will transfer quickly to the conduction band (CB) of BOC and cause the vibration of local oxygen atoms, thus leading to the compressive stress from the surrounding grains [29,30]. This unique effect also suggests the existence of Au NPs.

SEM images of pure BOC SCNSs and Au/BOC samples are shown in Fig. 2. As can be seen in Fig. 2(a) and (c), the as-synthesized BOC SCNSs consist of large-scale sheet-shaped structures with a micrometer-scale width and an average thickness of 50–200 nm. Also, Au deposition process brought no observable change to the morphology of the BOC samples (Fig. 2b and d). As to determine the exposed facet of BOC SCNSs and inspect the distribution of Au NPs, TEM analyses were conducted and the results are displayed in Fig. 3. It is observed that Au NPs were deposited randomly onto the surface of the samples (see Fig. 3a and c). The sizes of Au NPs on two facets were also calculated by reviewing more than 50 particles. As can be seen in the insets of Fig. 3a and c, particle sizes of Au NPs loaded on two facets are of resemblance and range from 2 to 14 nm. The average sizes of Au NPs are both around 6 nm. High-resolution TEM (HRTEM) images in Fig. 3b and d reveal the high crystallinity of both the BOC SCNSs. In the BOC sample synthesized at pH = 6.0 (Fig. 3d), HRTEM analysis clearly reveals the presence of (0 0 2) and (1 0 2) crystallographic planes with lattice space of 0.368 and 0.267 nm, respectively. The angle indicated by the corresponding SAED results (Fig. 3d, inset) is 43.4°, which is identical to

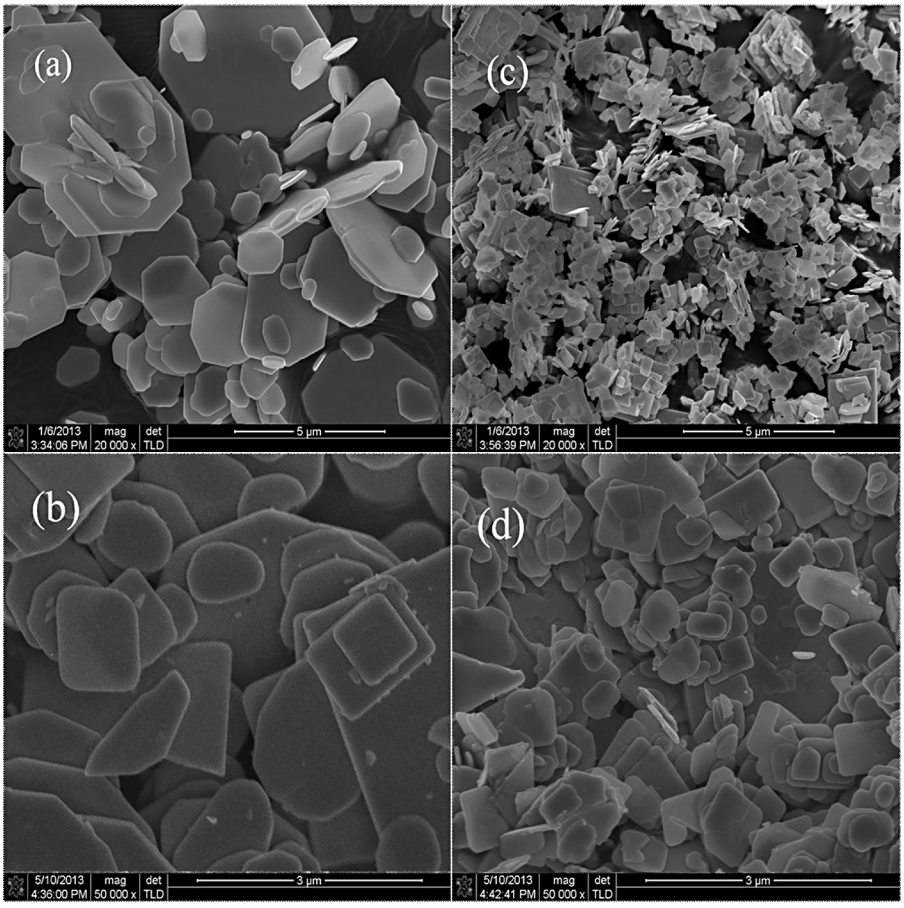

Fig. 2. SEM images of (a) BOC-001, (b) Au/BOC-001, (c) BOC-010, (d) Au/BOC-010.

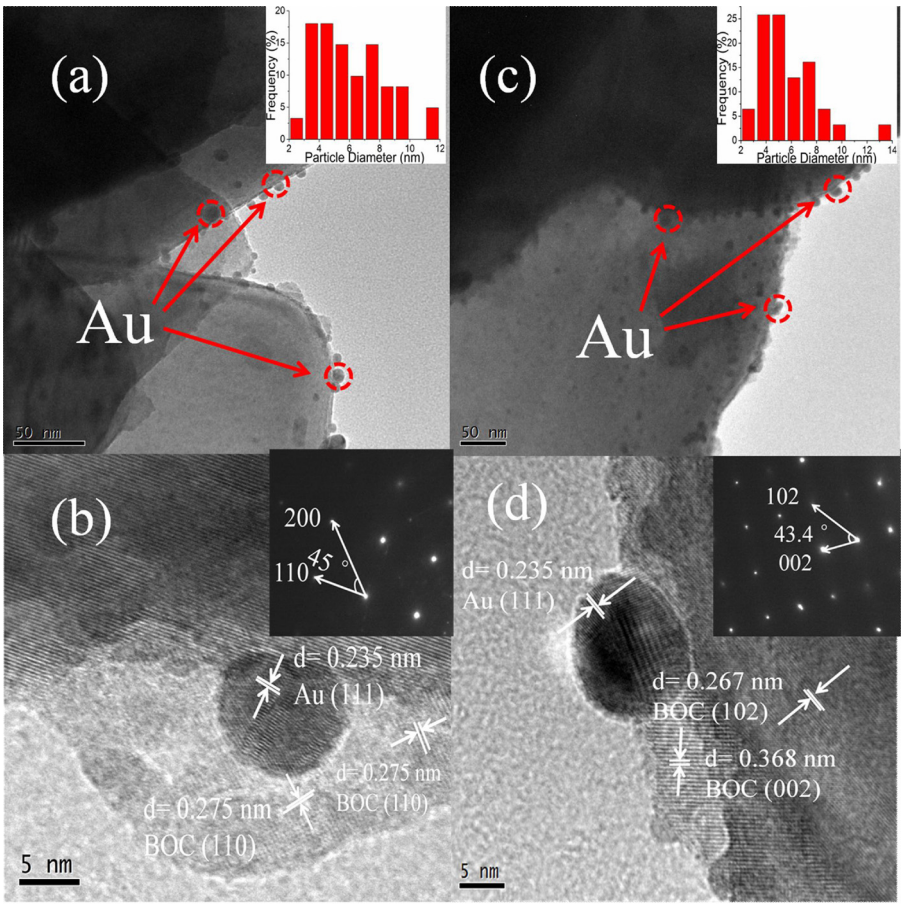

Fig. 3. TEM images and the Au particle size distribution of Au/BOC SCNSs: (a) Au/BOC-001 (the inset is the Au particle size distribution), (b) HRTEM image of Au/BOC-001 (the inset is the SAED), (c) Au/BOC-010 (the inset is the Au particle size distribution), (d) HRTEM image of Au/BOC-010 (the inset is the SAED).

the theoretical value of the angle between (0 0 2) and (1 0 2) faces. Both of the above results suggest that mainly exposed facets of BOC SCNSs prepared at pH = 6.0 are {0 1 0}. By contrast, in the BOC sample obtained without NaOH, the clear lattice fringes with an interplanar d-spacing of 0.275 nm correspond to the (1 1 0) atomic planes. The angle labeled in its SAED pattern is 45°, in agreement with that between (2 0 0) and (1 1 0). According to the symmetry of tetragonal BiOCl, the largely exposed plane can be undoubtably identified as {0 0 1} facets. As for the Au NPs, the disclosed lattice space of 0.235 nm conforms well to the characteristic d-value of (1 1 1) planes of Au crystal. Additionally, the chemical state of the surface gold atoms was determined by XPS analysis. To exclude any effect on the values of binding energy (BE) due to charging of the sample during the XPS analysis, all data were calibrated by adventitious C as reference (284.6 eV). 4f lines of Au loaded on BOC SCNSs are illustrated in Fig. 4. Two main peaks with BEs at 83.7 and 87.4 eV are ascribed to Au $4f_{7/2}$ and Au $4f_{5/2}$, respectively, which denotes that Au particles are in their metallic state [25,31,32].

3.2. Photocatalytic activity under intrinsic excitation

The success in controlling the facet exposure of BOC SCNSs and the deposition Au NPs allowed us to investigate the facet-dependent PTO of charge carriers and the influence of Au NPs over photocatalytic activity. Here, we evaluated the performance of the samples by degradation reaction and Orange II, a typical azo dye, was used as a model pollutant. Shown in Fig. 5(a) is the evolvement of the UV–vis absorption of Orange II under UV light (mainly 254 nm) irradiation. Negligible amount of the azo dye was decomposed by photolysis after 2 h while all the dye molecules were degraded with the presence of photocatalyst in the same period. It is interesting to note that, when loaded with Au NPs, the activity of BOC-001 sample was promoted whereas the BOC-010 one showed an obvious decline. This contradictory effect is even more noticeable after transformation by pseudo-first-order kinetics (Fig. 5(b)). In a general way, the Schottky barrier between noble metal and semiconductor is beneficial for the separation of charge carriers and this separation will promote the photocatalytic activity

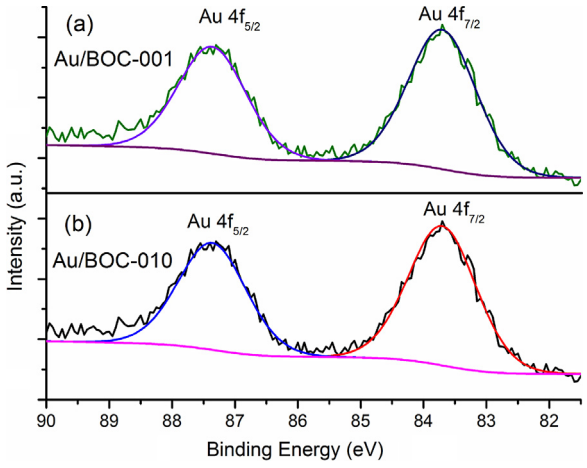

Fig. 4. XPS results for Au NPs on BOC SCNSs with different facets: (a) Au/BOC-001, (b) Au/BOC-010.

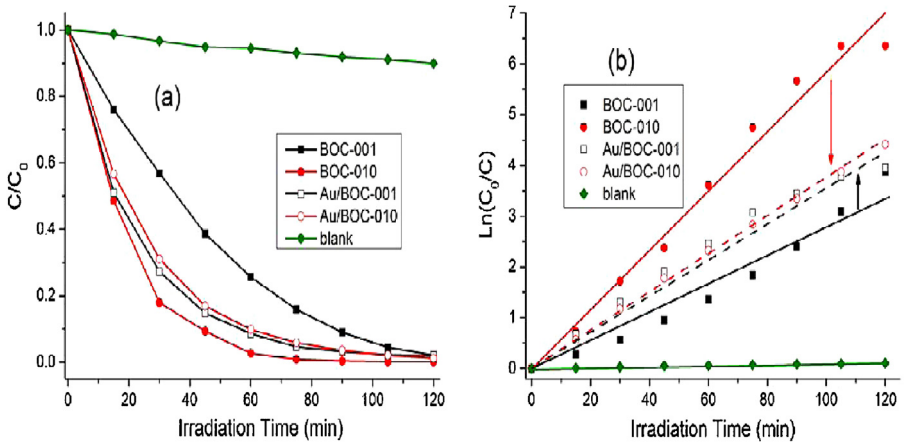

Fig. 5. Photodegradation of Orange II under UV light irradiation: (a) Variations of concentration of Orange II during degradation process; (b) Fitting results using pseudo-first-order kinetics.

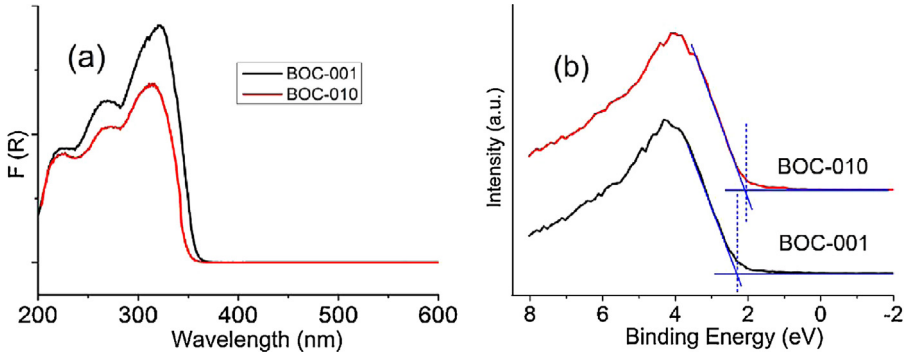

Fig. 6. (a) Diffuse-reflectance spectra of BOC-001 and BOC-010 and (b) valence band XP spectra of BOC-001 and BOC-010.

[16–18]. Nevertheless, the reverse phenomenon here indicates that Au NPs on the (010) facet may have caused the recombination of some e^-–h^+ pairs, just like that in TiO_2 with different facets [8,33]. These results indicate that there may be the PTO for different charge carriers in the present system, by which photo-generated electrons and holes are spontaneously driven toward different crystal facets in the photochemical process.

3.3. PTO of charge carriers in facet-oriented BOC

In essence, the distinction in the PTO of different charge carriers is inherently determined by electronic energy levels of a certain material [8]. In this work, DRS results in Fig. 6a reveal that the corresponding band gaps for BOC-001 and BOC-010 are 3.42 and 3.54 eV, and the band absorption of BOC-001 has a red-shift for about 10 nm with respect to that of BOC-010. Obviously, the higher percentage of {0 0 1} in BOC-001 is responsible for this red-shift. XPS valence band (VB) spectra (Fig. 6b) further indicate that the VB maxima of BOC-001 and BOC-010 are at 2.3 and 2.1 eV, accordingly, the CB minimum of BOC-010 is raised in contrast to BOC-001. Similar subtle difference in the band gap caused by different exposed facets has been well studied in TiO_2 system [34]. Here, according to the distinct electronic band structures of BOC-001 and BOC-010, the PTO is thermodynamically feasible and the proposed mechanism is shown in Fig. 7. When BOC SCNSs are activated by intrinsic excitation, electrons tend to transfer to {0 0 1} facets and the holes are prone to migrate to {0 1 0} facets, which results in the reduction ({0 0 1}) and oxidation ({0 1 0}) faces. In the case of Au deposition, the electrons will then be unidirectionally driven to sink on Au NPs due to the Schottky junction on the interface, which will facilitate the electron transfer on (0 0 1) face or cause recombination on (0 1 0) plane.

The above analyses were further supported by transient photocurrent response of the samples in several on/off cycle tests under intermittent UV light irradiation. Fig. 8 compares the *I*–*t* curves of different samples and a good reproducibility of photocurrent is observed. In common sense, the initial current results from the separation of electron–hole pairs at the BOC/electrolyte

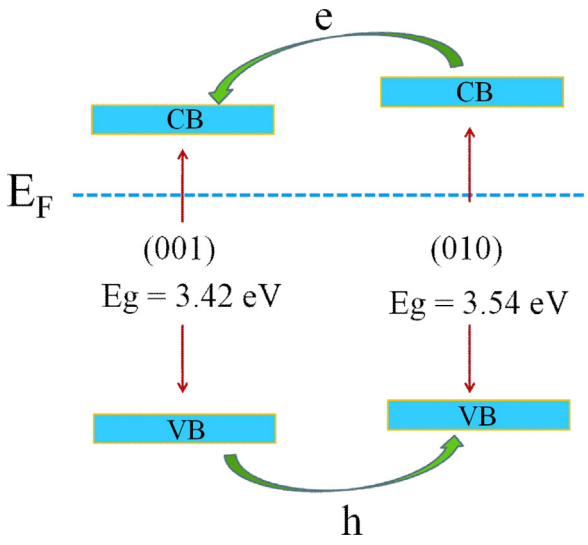

Fig. 7. The proposed mechanism of the facet-induced PTO.

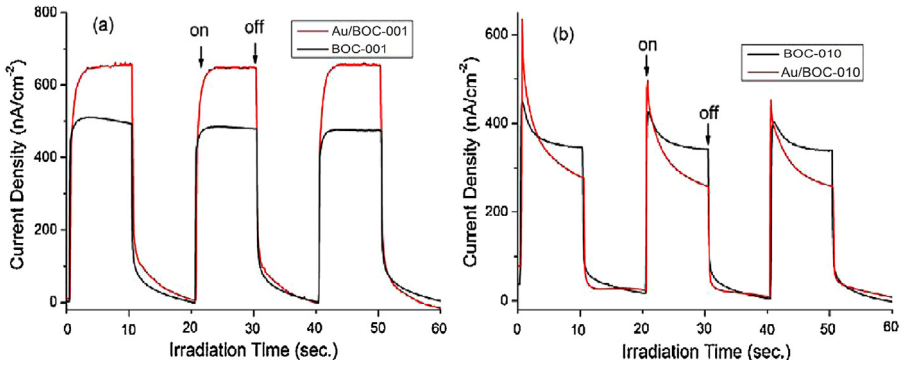

Fig. 8. Comparison of transient photocurrent response of BOC SCNSssamples: (a) BOC-001 and Au/BOC-001, (b) BOC-010 and Au/BOC-010.

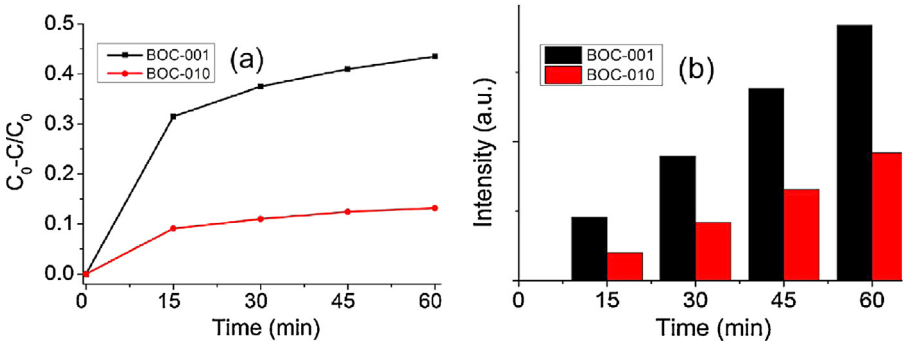

Fig. 9. The spectra of active oxygen radicals generated during BOC-001 and BOC-010 photocatalysis under UV light irradiation (a) the generation of $O_2^{\bullet-}$ (b) the generation of $^{\bullet}OH$.

interface, during which photo-generated holes migrating to BOC SCNSs surface are trapped or captured by reduced species in the electrolyte while the electrons are transported to the back contact substrate *via* BOC SCNSs [35,36]. The photocurrent value of pure BOC-001 increased for about 30% after Au deposition as illustrated in Fig. 6a, indicating charge separation in the photoelectrochemical process has been promoted, which is in accord with the activity results. Also, the current is steady within the whole illumination period, implying that there is little recombination process. On the contrary, as shown in Fig. 6b, the photocurrent curves of all BOC-010 samples have an anodic photocurrent spike at the initial time of irradiation. After that, a gradual and continuous decay is observed, revealing recombination processes of photo-induced electrons and holes are occurring [36]. From the perspective of carriers, two reasons are to be considered here. One is that holes may accumulate at the surface and then discharge with electrons from the conduction band of BOC SCNS rather than capture electrons from the electrolyte. Another reason is that CB electrons start to reduce photo-generated oxidized species in the electrolyte [35–37]. For Au/BOC-010 sample, the higher initial current is ascribed to Schottky barrier between Au and BOC-010, which gives rise to electron transfer from BOC-010 to Au NPs. However, the decline curve is sharper than that of bare BOC-010, revealing a more excessive recombination. As the majority of electrons are transferred to Au NPs surface, the interaction between Au and holes is responsible for the decay, that is, except for some of the generated holes that are trapped at the interface, the others migrate to the negatively charged Au NPs due to the interactive Coulomb force [18]. The holes passing through the barrier then lead to the recombination of electron–hole pairs, and eventually resulted in a lower current signal. Therefore, the contradictory photocurrents caused by Au deposition firmly demonstrate the (0 0 1) facet is the electron-preferred (reductive) facet and (0 1 0) facet is the hole-preferred (oxidative) one.

3.4. Detection of primary active species during the photocatalytic process

To elucidate the photodegradation mechanism of BOC SCNSs, the reactive oxidative species (ROS) generated by pure BOC samples with distinct energy levels were tested. It is generally accepted that $O_2^{\bullet-}$ and $^{\bullet}OH$ radicals as well as photo-generated holes are the main ROS in photocatalytic degradation reactions. Here, we first compared the generation capability of $O_2^{\bullet-}$ and $^{\bullet}OH$ radicals of different pure BOC SCNSs under UV light irradiation. A colorless molecular probe NBT was used to quantify the $O_2^{\cdot-}$ and TA was chosen to detect the amount of ·OH [22,23,38]. As exhibited in Fig. 9, the as-synthesized BOC samples show different abilities for generating $O_2^{\bullet-}$ radicals and a discrepancy is also observed in their $^{\bullet}OH$ evolution rates upon normalization by the surface area, where the $O_2^{\bullet-}$ radicals and $^{\bullet}OH$ evolution rates are higher in the BOC-001 system than that in the BOC-010. However, according to the XPS results studying the VB of BOC SCNS, both the VB maxima of BOC-001 and

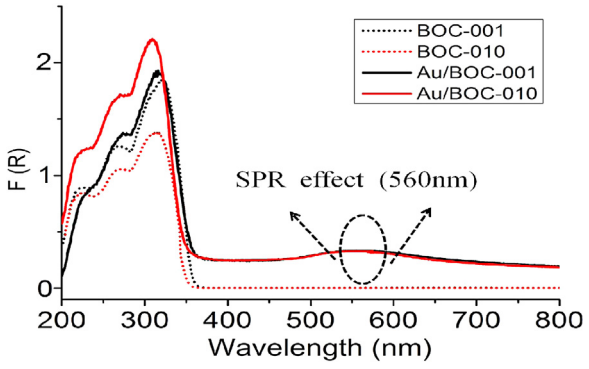

Fig. 10. Diffuse-reflectance spectra of BOC SCNSs and Au/BOC SCNSs.

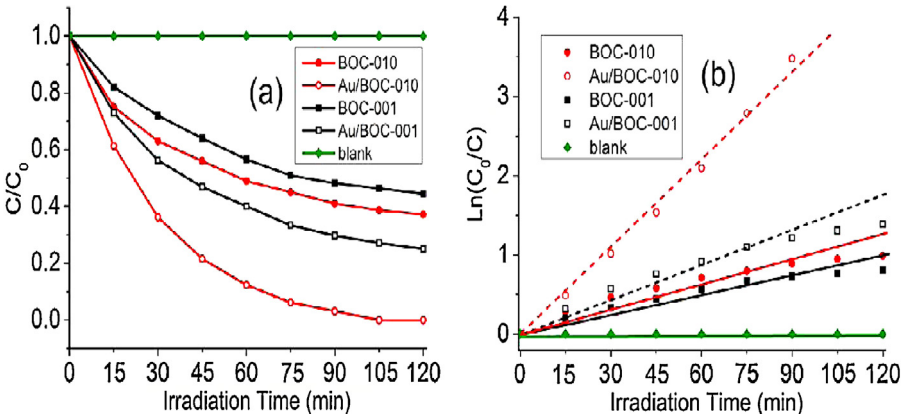

Fig. 11. Time course of the decrease in the concentration (a) and $\ln(C_0/C)$ (b) for the photodegradation of Orange II under vis-irradiation.

BOC-010 are energetically insufficient to generate hydroxyl radicals [39,40]. Thus, the $^{\bullet}OH$ species are reasonably derived from $O_2^{\bullet-}$, during which the H_2O_2 are also generated as a necessary intermediate [39]. To further inspect the H_2O_2 species, DPD/POD method is used to qualify the generation of H_2O_2 *in situ*, as H_2O_2 will oxidize POD to a higher valent state, which in turn oxidizes DPD to a pink colored radical cation-DPD$^{\bullet+}$, stabilized by resonance with absorption maxima at 510 and 551 nm [24,41]. Here again, there is a higher concentration of H_2O_2 in the BOC-001 system upon normalization by the surface area as presented Fig. S2. Nevertheless, despite that much more ROS ($O_2^{\bullet-}$, $^{\bullet}OH$ and H_2O_2) are generated from BOC-001, its inferior photocatalytic performance manifests that photo-induced holes are vital to the degradation, which is exactly the reason why pure BOC-010 depicts superior degradation activity.

3.5. Optical properties of the Au loaded BOC samples

Fig. 10 shows the DRS results of BOC SCNSs before and after Au loading. In contrast to their respective referenced sample, a clear absorption at approximately 550 nm in the visible region is observed in Au/BOC SCNSs, which is attributed to the typical plasmon resonance absorption of Au NPs. It has been reported that the band position and intensity of the plasmon absorption depends on the particle size and the amount of gold particles, respectively [22,42]. The DRS analyses impart that the two characteristics of the Au loaded samples are of resemblance, indicating both Au NPs on the BOC-001 and BOC-010 sample share the similar loading amount as well as an average particle size. This result is in good accordance with the presentation of the above TEM analyses (Fig. 3a and c). Simultaneously, the absorption in the ultraviolet region is also enhanced due to the Au particles-induced light scattering [18,20].

3.6. Visible light activity induced by SPR effect and the influence of substrate facets

In addition to the promotion effect in the separation of charge carriers, Au NPs are also widely investigated as a promising plasmonic photocatalyst due to their unique SPR effect, which renders wide gap semiconductors with visible light activity [18,43–45]. However, the SPR effect is reported to be inseparably affected by the substrate support [21,22]. In the light of the subtle distinction of the various atomic configurations and the electronic energy levels of BOC SCNSs in the present study, the SPR effect may also be influenced by the exposed facets. For this reason, the photocatalytic activity of Au/BOC system is investigated.

Fig. 11 is the photocatalytic degradation process of all samples under visible light irradiation. The Orange II molecule is quite stable under visible light illumination. A part of the azo dye are decomposed through an indirect dye photosensitization degradation process in the presence of BOC catalyst, while both the activity of pure BOC is enhanced after Au deposition due to the SPR effect [18–20,43–45]. Noticeably, the photocatalytic activity rate of Au/BOC-010 was enhanced by a factor of 3.5 as compared with bare BOC-010 sample, whereas this value is only about 1.6 in the (0 0 1) couple. The discernable promoting difference is reasonably attributed to the different substrates of Au.

It is widely acknowledged that, in the plasmon-induced photocatalytic process, upon the excitation of Au NPs, the electrons from Au NPs are injected into the conduction band of the substrate semiconductor, which further reduce the adsorbed oxygen to generate the $O_2^{\bullet-}$ radicals. In the present system, the outmost layer of BOC (0 0 1) face is constituted by O atoms, and that on the (0 1 0) is a periodical arrangement of Bi, O and Cl ternary composite (see Fig. 12). The unique open channel structure on (0 1 0) face provides many adsorption sites for the azo dye [14], which can effectively shortened the diffusion distance of transient $O_2^{\bullet-}$ species. This also accounts for the better activity of bare BOC-010 with respect to BOC-001 in degradation of Orange II. On the other hand, a stronger metal/support interaction is beneficial for prompt and efficient interfacial charge transfer, as an intimate contact will evidently facilitate the transfer process [22,46,47]. Here, the binding energy of Bi 4f is investigated and the results are displayed in Fig. 13. After fitting, Bi 4f spectra of bare samples are composed of two peaks at the binding energies of 158.9 and 164.2 eV, assign to Bi $4f_{7/2}$ and Bi $4f_{5/2}$ respectively, suggesting the presence of Bi^{3+} [48]. After Au loading, an obvious shift for about 0.2 eV toward the higher BE can be noticed in both peaks of the Au/BOC-010 sample in comparison to original BOC-010 sample, while the two peaks of the BOC-001 couple remained unchanged. This shift is an indication that the interfacial interaction between Au and BOC-010 is stronger than that in the Au/BOC-001 system [22]. Considering that the cause by Au particle size and amount are excluded in the present

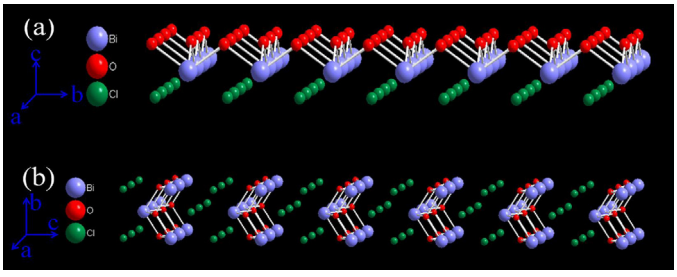

Fig. 12. Atomic structure of {0 0 1} (a) and {0 1 0} (b) facets with side view.

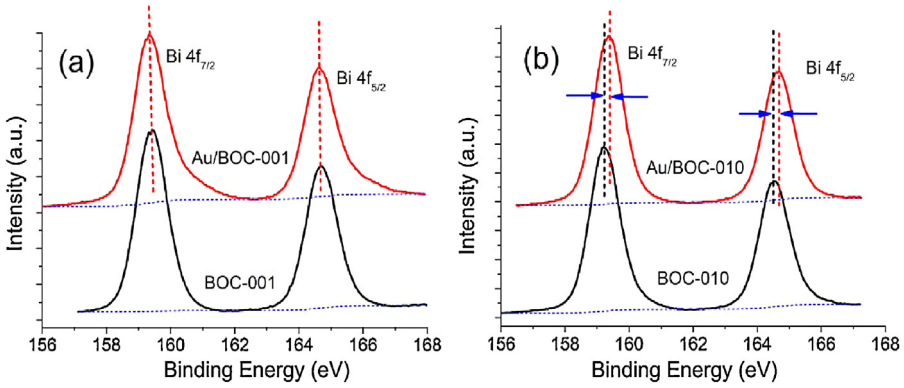

Fig. 13. The comparison of XPS results for Bi 4f (a) BOC-001 and Au/BOC-001, (b) BOC-010 and Au/BOC-010.

system, we believe that the unique channel structure and the intense interfacial interaction between Au and BOC (0 1 0) facet could act cooperatively to achieve a more pronounced visible light activity of Au/BOC-010.

4. Conclusions

Summarily, BOC SCNSs with dominant exposed (0 0 1) and (0 1 0) facets were synthesized and metallic Au NPs were successfully deposited onto the BOC surface by chemical reduction method. The PTO of photo-generated carriers in BOC material was investigated and it was demonstrated electrons and holes would transfer spontaneously toward (0 0 1) and (0 1 0) facet, respectively. Photo-induced holes and $O_2^{\bullet -}$ species, as well as the derived $^{\bullet}OH$ radicals, acted as the main ROS in the degradation of Orange II by BOC photocatalyst. Moreover, it was revealed that the interaction between Au and (0 1 0) facet of BOC is stronger than that on the BOC (0 0 1) face, which resulted in an enhanced visible light activity induced by SPR effect.

Acknowledgements

This work was financially supported by NSFC (Grants U1305242, Nos. 21373051 and 21173044), the great Science and Technology Project of Fujian Province of PR China (2012Y4003).

Appendix A. Supplementary data

Supplementary data associated with this article can be found, in the online version, at http://dx.doi.org/10.1016/j.apcatb.2014.05.018.

References

[1] X. Han, Q. Kuang, M. Jin, Z. Xie, L. Zheng, J. Am. Chem. Soc. 131 (2009) 3152–3153.
[2] N. Zhang, M. Yang, Z. Tang, Y. Xu, J. Catal. 303 (2013) 60–69.
[3] G. Li, B. Jiang, X. Li, Z. Lian, S. Xiao, J. Zhu, D. Zhang, H. Li, ACS Appl. Mater. Interf. 5 (2013) 7190–7197.
[4] M.D. Arienzo, J. Carbajo, A. Bahamonde, M. Crippa, S. Polizzi, R. Scotti, L. Wahba, F. Morazzoni, J. Am. Chem. Soc. 133 (2011) 17652–17661.
[5] N. Wu, J. Wang, D.N. Tafen, H. Wang, J.G. Zheng, J.P. Lewis, X. Liu, S.S. Leonard, A. Manivannan, J. Am. Chem. Soc. 132 (2010) 6679–6685.
[6] A. Riss, M.J. Elser, J. Bernardi, O. Diwald, J. Am. Chem. Soc. 131 (2009) 6198–6206.
[7] C. Liu, X. Han, S. Xie, Q. Kuang, X. Wang, M. Jin, Z. Xie, L. Zheng, Chem. Asian J. 8 (2013) 282–289.
[8] R. Li, F. Zhang, D. Wang, J. Yang, M. Li, J. Zhu, X. Zhou, H. Han, C. Li, Nat. Commun. 4 (2013) 1432–1438.
[9] G.G. Briand, N. Burford, Chem. Rev. 99 (1999) 2601–2657.
[10] S. Zhou, Y. Ke, J. Li, S. Lu, Mater. Lett. 57 (2003) 2053–2055.
[11] S. Wu, C. Wang, Y. Cui, T. Wang, B. Huang, X. Zhang, X. Qin, P. Brault, Mater. Lett. 64 (2010) 115–118.
[12] L. Chen, S. Yin, R. Huang, Y. Zhou, S. Luo, C. Au, Catal. Commun. 23 (2012) 54–57.
[13] L. Ye, L. Zan, L. Tian, T. Peng, J. Zhang, Chem. Commun. 47 (2011) 6951–6953.
[14] J. Jiang, K. Zhao, X. Xiao, L. Zhang, J. Am. Chem. Soc. 134 (2012) 4473–4476.
[15] J. Jang, L. Zhang, H. Li, W. He, J.J. Yin, Nanoscale 5 (2013) 10573–10581.
[16] W. Wu, L. Liao, S. Zhang, J. Zhou, X. Xiao, F. Ren, L. Sun, Z. Dai, C. Jiang, Nanoscale 5 (2013) 5628–5636.
[17] M. Pang, J. Hu, H.C. Zeng, J. Am. Chem. Soc. 132 (2010) 10771–10778.
[18] K. Liu, M. Sakurai, M. Liao, M. Aono, J. Phys. Chem. C 114 (2010) 19835–19839.
[19] E. Kowalska, R. Abe, B. Ohtani, Chem. Commun. 2 (2009) 241–243.
[20] J. Lu, P. Zhang, A. Li, F. Su, T. Wang, Y. Liu, J. Gong, Chem. Commun. 49 (2013) 5817–5819.
[21] S. Zhu, S. Liang, Q. Gu, L. Xie, J. Wang, Z. Ding, P. Liu, Appl. Catal. B: Environ. 119–120 (2012) 146–155.
[22] K. Cheng, W. Sun, H. Jiang, J. Liu, J. Lin, J. Phys. Chem. C 117 (2013) 14600–14607.
[23] L. Ye, J. Mao, J. Liu, Z. Jiang, T. Peng, L. Zan, J. Mater. Chem. A 1 (2013) 10532–10537.
[24] Y. Pi, L. Zhang, J. Wang, J. Hazard. Mater. 141 (2007) 707–712.
[25] H. Li, Z. Bian, J. Zhu, Y. Huo, H. Li, Y. Lu, J. Am. Chem. Soc. 129 (2007) 4538–4539.
[26] H. Xia, Y. Wang, F. Kong, S. Wang, B. Zhu, X. Guo, J. Zhang, Y. Wang, S. Wu, Sens. Actuators B 134 (2008) 133–139.
[27] J. Geng, W. Hou, Y. Lv, J. Zhu, H. Chen, Inorg. Chem. 44 (2005) 8503–8509.
[28] Y. Lei, G. Wang, S. Song, W. Fan, H. Zhang, CrystEngComm 11 (2009) 1857–1862.
[29] L. Zhang, W. Wang, S. Sun, Y. Sun, E. Gao, J. Xu, Appl. Catal. B: Environ. 132–133 (2013) 315–320.
[30] S. Cao, C. Guo, Y. Lv, Y. Guo, Q. Liu, Nanotechnology 20 (2009) 275702.
[31] A. Zwijnenburg, A. Goossens, W.G. Sloof, M.W.J. Crajé, A.M. van der Kraan, L.J. Jongh, M. Makkee, J.A. Moulijn, J. Phys. Chem. B 106 (2002) 9853–9862.
[32] T.F. Jaramillo, S.H. Baeck, B.R. Cuenya, E.W. McFarland, J. Am. Chem. Soc. 125 (2003) 7148–7149.
[33] C. Liu, X. Han, S. Xie, Q. Kuang, X. Wang, M. Jin, Z. Xie, L. Zheng, Chem. Asian J. 8 (2013) 282–289.
[34] J. Pan, G. Liu, G. Lu, H. Cheng, Angew. Chem. Int. Ed. 50 (2011) 2133–2137.
[35] J. Yu, G. Dai, B. Huang, J. Phys. Chem. C 113 (2009) 16394–16401.
[36] J. Yu, B. Wang, Appl. Catal. B: Environ. 94 (2010) 295–302.
[37] J. Yu, S. Liu, H. Yu, J. Catal. 249 (2007) 59–66.
[38] Y. Yu, C. Cao, H. Liu, P. Li, F. Wei, Y. Jiang, W. Song, J. Mater. Chem. A 2 (2014) 1677–1681.
[39] M.R. Hoffmann, S.T. Martin, W. Choi, D.W. Bahnemann, Chem. Rev. 95 (1995) 69–96.
[40] Z. Li, T. Dong, Y. Zhang, L. Wu, J. Li, X. Wang, X. Fu, J. Phys. Chem. C 111 (2007) 4727–4733.
[41] T. Wu, G. Liu, J. Zhao, H. Hidaka, N. Serpone, J. Phys. Chem. B 103 (1999) 4862–4867.
[42] P. Claus, A. Bruckner, C. Mohr, H. Hofmeister, J. Am. Chem. Soc. 122 (2000) 11430–11439.
[43] Q. Xiang, G.F. Meng, H.B. Zhao, Y. Zhang, H. Li, W.J. Ma, J.Q. Xu, J. Phys. Chem. C 114 (2010) 2049–2055.
[44] D. Tsukamoto, Y. Shiraishi, Y. Sugano, S. Ichikawa, S. Tanaka, T. Hirai, J. Am. Chem. Soc. 134 (2012) 6309–6315.
[45] Z. Chu, C. Yin, S. Zhang, G. Lin, Q. Li, Nanoscale 5 (2013) 3406–3411.
[46] V. Subramannian, E.E. Wolf, P.V. Kamat, J. Am. Chem. Soc. 126 (2004) 4943–4950.
[47] C.G. Silva, R. Juarez, T. Marino, R. Molinari, H. Garicia, J. Am. Chem. Soc. 133 (2011) 595–602.
[48] S. Peng, L. Li, P. Zhu, Y. Wu, M. Srinivasan, S.G. Mhaisalkar, S. Ramakrishna, Q. Yan, Chem. Asian J. 8 (2013) 258–268.